Hwang et al. *NPG Asia Materials* (2023) 15:29
https://doi.org/10.1038/s41427-023-00476-x

NPG Asia Materials

ARTICLE Open Access

$Ti_3C_2T_x$ MXene as a growth template for amorphous RuO_x in carbon nanofiber-based flexible electrodes for enhanced pseudocapacitive energy storage

Hyewon Hwang[1], Sungeun Yang[2], Seoyeon Yuk[1], Kug-Seung Lee[3], Segi Byun[4] and Dongju Lee[1,5]

Abstract

A noble surface engineering method was developed to create a binder-free flexible electrode comprising $Ti_3C_2T_x$ MXene/carbon nanofibers (MCNFs) covered by amorphous RuO_x with a combined electrospinning and hydrothermal process. Utilizing the hydrophilicity of the MXene on/in the MCNFs, RuO_x was easily coated on the surfaces of the MCNFs through oxygen-mediated chemical bonding between the functional groups of the MXene and Ru ions. A structural analysis revealed that the MXene acted as a growth template for RuO_x and that the formed RuO_x had an amorphous and disordered state in the composite electrode, which impacted the electrochemical performance. The electrochemical tests showed that these composite electrodes improved the electrochemical performance, with a two-fold increase in the gravimetric capacitance (279.4 F/g at 2 mV/s) relative to that of pristine MCNFs, a wide potential window (from 0.7 to 1 V) providing a superior energy density of 8.5 Wh/kg at a power density of 85.8 W/kg, as well as long-term cycling stability (99% after 10,000 cycles). The synergetic effect of the RuO_x and MXene in the composite electrodes was attributed to an enhanced pseudocapacitive reaction. Our novel electrodes and fabrication method confirm the great potential of CNF-based composites for the development of high-performance binder-free electrodes for supercapacitors.

Introduction

There is increasing demand for supercapacitors as electrochemical energy storage devices. Due to their rapid charge/discharge derived from high power densities, superior rate capabilities, and excellent long cycling life, supercapacitors are important devices for many applications, such as electric vehicles, drones, and military equipment operating in low-temperature environments and conditions with high power requirements[1–5]. These devices can be classified into two types according to their charge storage mechanisms: electric double-layer capacitors and pseudocapacitors. Electric double-layer capacitors store energy by using a double layer of electrolyte ions on the surfaces of the electrodes. Although typical electrodes made from carbonaceous materials have long-term stability, electric double-layer capacitors are limited by intrinsic low capacitance because of their surface-only reactions. In contrast, for pseudocapacitors, the electrical charge is stored via either a surface adsorption/desorption process or a fast and reversible surface redox reaction. Although electrodes made of conducting polymers[6] or metal oxides[7,8] provide enhanced capacitance[1], they exhibit low conductivities or poor cycling stabilities[9]. Therefore, there is a need to develop a composite

Correspondence: Segi Byun (segibyun@kier.re.kr) or
Dongju Lee (dongjulee@chungbuk.ac.kr)
[1]Department of Urban, Energy, and Environmental Engineering, Chungbuk National University, Chungdae-ro 1, Seowon-Gu, Cheongju, Chungbuk 28644, Republic of Korea
[2]Center for Energy Materials Research, Korea Institute of Science and Technology (KIST), 5, Hwarang-ro 14-gil, Seongbuk-gu, Seoul 02792, Republic of Korea
Full list of author information is available at the end of the article

electrode exhibiting a high capacitance, superior rate performance, and long-term cycle stability. Such electrodes are typically made by compounding carbon-based materials decorated with highly conductive or redox-active materials, such as MXene[10], MnO_2[11], $Ni(OH)_2$[12], and RuO_2[13].

As with other carbon-based materials, electrospun carbon nanofibers (CNFs) suffer from limited capacitance and poor performance, even though they are flexible without including binding polymers; they also exhibit acceptable capacitance (~100 F/g) for high power demands, and easy and cost-effective fabrication. To overcome these limitations, highly capacitive and conductive materials have been introduced into CNF-based electrodes by various methods[14–21]. Several methods are available for the fabrication of CNF-based composite electrodes with various metal oxides[16,22–24]. However, pristine CNFs have insufficient surface functional groups to anchor metals or metal oxides during processing, so the metal precursors are typically introduced into a polymer solution to produce polymer nanofiber/metal oxide composites as the source of the CNF/metal oxide composite electrodes. However, these fabrication protocols not only lead to unintended growth of the metal oxide particles, such as aggregated forms or byproduct particles with different compositions in the composites, but also make it difficult to control the mass loading of the metal oxides in the composites. Therefore, precise control of the metal oxide loading and development of a synthetic protocol for conformal decoration of particles grown on CNF-based electrodes are essential for boosting the electrochemical performance with high gravimetric capacity and extremely stable device operation.

Among composite materials, MXenes, a family of two-dimensional materials consisting of transition metal carbides and/or nitrides, are considered to be suitable nanofillers for energy storage and conversion because they promote electron transfer due to their unique properties, which include metallic conductivity for effective electrochemical performance and hydrophilicity to facilitate hydrothermal treatment[25,26]. In producing CNF composite electrodes with enhanced electrochemical performance, we recently introduced a $Ti_3C_2T_x$ MXene conductive agent into PAN-based electrospun CNFs to prepare MXene-wrapped CNF (MCNF) flexible electrodes[20]. These composite electrodes showed enhanced capacitances up to 120 F/g (at 2 mV/s) and improved rates. However, the low energy density of the composites incorporated with MXenes, which was derived from the narrow potential window (~0.7 V) of the $Ti_3C_2T_x$ MXene, restricted the utility for high energy storage applications.

RuO_2 has been used as an additional pseudocapacitive material in MCNFs to boost the energy density of the CNF-based electrode because of its remarkably high specific capacitance, good electrical conductivity, reversible charge/discharge capability, and wide potential window[27–29]. Moreover, amorphous RuO_2 (RuO_x) would be of particular interest as an electrode material for pseudocapacitors because of its metallic conductivity, a specific capacitance (720 F/g) higher than that of crystalline RuO_2 (144–530 F/g)[30], and highly reversible redox reactions[31,32]. As mentioned above, it is difficult to directly hybridize a pristine CNF electrode with RuO_2 due to the limited availability of functional groups. Therefore, a method is needed for incorporating $Ti_3C_2T_x$ MXene into CNFs as a growth template for other pseudocapacitive materials, such as RuO_2.

Here, we present a simple and effective hydrothermal treatment method for improving the electrochemical performance of CNF-based electrodes by utilizing $Ti_3C_2T_x$ MXene as a growth template for RuO_x in CNF-based electrodes. Utilizing the functionality of the MXenes on/in the MCNFs, RuO_x was grown on the surface of the MXene in the MCNF through strong chemical coupling between the functional groups of MXene and Ru; the MXene acted as a template for RuO_x particle growth, and the resulting RuO_x was amorphous and disordered in the composite electrode, which had a positive impact on the electrochemical performance. In addition, the RuO_x mass loading in the composite was easily adjusted while retaining its fiber morphology, and the electrochemical performance could be optimized by regulating the amount of RuO_x in the composites. A woven free-standing composite electrode was fabricated with a symmetric supercapacitor device in an aqueous electrolyte, and it showed high gravimetric capacitance, low electrical resistance, good rate capability at high scan rates, a broad potential window, and excellent cycling stability over 10000 (10 K) charge/discharge cycles. This simple method utilizing the $Ti_3C_2T_x$ MXene as a growth template for a third element is an effective means of improving the electrochemical performance of CNF-based composite and binder-free electrodes and can be used to prepare flexible supercapacitors.

Materials and methods

Synthesis of the $Ti_3C_2T_x$ MXene

Ti_3AlC_2 MAX phase powder (particle size ≤ 38 μm) was purchased from Carbon–Ukraine Ltd. and subjected to selective etching of Al as follows. Lithium fluoride (1.6 g; Sigma–Aldrich, Korea) was slowly dissolved in 20 mL of 9 M HCl (Samchun Chemical, Korea). Ti_3AlC_2 powder (1.0 g) was slowly added to the solution; the mixture was stirred at 500 rpm for 24 h at room temperature. The suspension was washed several times by centrifugation at 3500 rpm with deionized water (DIW) until reaching pH ≥ 6. Then, the sediment was redispersed in 150 mL of DIW, and the solution was centrifuged at 5000 rpm for

1 h. The supernatant was removed, and the remaining $Ti_3C_2T_x$ MXene sheets were freeze-dried for use in electrospinning dope solution.

Preparation of the $Ti_3C_2T_x$ MCNFs

Typically, 200 mg of $Ti_3C_2T_x$ was dissolved in dimethylformamide (Samchun Chemical) by bath sonication. Then, 800 mg of polyacrylonitrile (PAN; M_w 150,000; Sigma–Aldrich) was added to the solution with stirring at 80 °C for 8 h to obtain a homogeneous 10 wt% solution of PAN in dimethylformamide. The prepared $Ti_3C_2T_x$/PAN solution was transferred into a disposable plastic syringe equipped with an 18-gauge needle. The voltage between the needle tip and collector was 18 kV. The tip-to-collector distance was maintained at 15 cm; the feeding rate of the solution was 1.5 mL/h. The electrospun $Ti_3C_2T_x$/PAN nanofibers were peeled from the collector and stabilized at 280 °C for 1 h in air at a heating rate of 2 °C/min. Then, the preoxidized electrospun mat was carbonized at 800 °C for 1 h in an Ar atmosphere at a heating rate of 5 °C/min.

Coating of RuO_x on the $Ti_3C_2T_x$ MCNFs

The RuO_x-MCNFs were obtained with a hydrothermal reaction. First, specific amounts of $RuCl_3{\cdot}xH_2O$ were dissolved in DIW. Second, the as-prepared MCNFs were immersed in the $RuCl_3$ solution, transferred to a stainless-steel hydrothermal autoclave and heated in a box furnace at 150 °C for 10 h. The reacted samples were washed several times with DIW and then dried in a vacuum oven at 40 °C overnight. Finally, the samples were annealed in air at 200 °C for 3 h. The amount of Ru precursor relative to the MCNFs was added in multiples of n; each electrode was denoted as Rn-MCNF, where $n = 4$, 8, 16, and 32 (mass ratio). For comparison, hydrothermally treated MCNFs were prepared without the addition of the Ru precursor; these were denoted as HT-MCNFs.

Materials characterizations

The microstructures of the $Ti_3C_2T_x$ and prepared electrodes were examined with field-emission scanning electron microscopy (Crossbeam 540; ZEISS) and transmission electron microscopy (JEM-ARM200F; JEOL). To investigate the morphology of the $Ti_3C_2T_x$ sheets, atomic force microscopy was conducted in noncontact mode (SPM-9700; Shimadzu). To investigate the hydrophilicities of the samples, the water contact angles were measured with a contact angle analyzer (Phoenix 300 TOUCH, SEO Co.). X-ray diffraction analyses were performed with a JP/SmartLab instrument operating at a power of 9 kW with Cu Kα radiation. X-ray photoelectron spectroscopy (XPS; Quantera II system; PHI) was carried out with a monochromated Al Kα X-ray beam (1486.6 eV) to characterize the functional groups of the $Ti_3C_2T_x$, nanofibers, and RuO_x-coated electrodes. Raman spectroscopy was performed with a micro-Raman spectrometer (RAMANtouch; Nanophoton) equipped with a 532-nm laser. X-ray absorption spectroscopy (XAS) was conducted at the 8 C Nano XAFS beamline of the Pohang Light Source. The Ru K-edge spectra were obtained in transmission mode; a reference Ru foil was concurrently measured to calibrate each sample. The data were processed and fitted using ATHENA and ARTEMIS software. Coordination numbers were derived by fixing the S_0^2 value, which was obtained by fitting the RuO_2 powder data.

Electrochemical measurements

All Rn-MCNF electrodes exhibited diameters of 12.7 mm and were evaluated with a two-electrode cell kit (PAT-cell; EL-Cell) in 1 M H_2SO_4 aqueous electrolyte. The gel electrolyte was prepared by dissolving 1 g of PVA (Sigma–Aldrich, MW ≈ 146,000) in 10 ml of DI water. After heating the solution to 75 °C, the PVA solution became transparent. After cooling to room temperature, 1 g of H_2SO_4 was added slowly to the solution under continuous stirring to produce a PVA-H_2SO_4 gel electrolyte. The gel electrolyte was stored in a vial under ambient conditions for further use. To prepare a flexible supercapacitor, two identical electrodes (1×2 cm^2) were assembled together by applying a PVA-H_2SO_4 gel electrolyte. After applying the gel electrolyte, the excess water was evaporated at least 3 times under ambient conditions, and final assembly was done on a PET film. A Pt foil (thickness ~ 20 μm) was used as the current collector, a polypropylene membrane (Celgard 2400) was used as the separator, and a PET film (thickness ≈ 100 μm) was used as the flexible substrate. All electrochemical measurements were carried out under ambient conditions using a potentiostat (SP-150; BioLogic Science Instruments). Cyclic voltammetry (CV) curves were obtained at scan rates ranging from 2 to 300 mV/s within a potential window of 0–0.7 V. Galvanostatic charge/discharge (GCD) curves were measured at constant current densities of 0.2–10 A/g. Electrochemical impedance spectroscopy (EIS) measurements were conducted at a bias of 0 V with a sine wave of 10 mV over the frequency range 100 kHz to 100 MHz. The gravimetric capacitance C_g was calculated from the CV and GCD curves using Eqs. (1) and (2):

$$C_g = \frac{2}{m\nu\Delta V}\int IdV \tag{1}$$

$$C_g = \frac{2I}{(dV/dt)} \tag{2}$$

where m is the mass of the electrode (g), ν is the scan rate (V/s), ΔV is the potential window (V), I is the discharge

current (A), and dV/dt is the slope of the constant discharge curve (V/s).

The energy and power density, E_g and P_g, respectively, were calculated with Eqs. (3) and (4):

$$E_g = \frac{1}{8} C_g \Delta V^2 \tag{3}$$

$$P_g = \frac{I \Delta V}{2m} \tag{4}$$

Results and discussion

Figure 1 schematically illustrates the overall procedure used for the syntheses of the binder-free and free-standing RuO_x-MCNF electrodes. The MXene was adequately etched from the Ti_3AlC_2 MAX phase (Fig. S1); it had a lateral size of <1 μm (Fig. S2) and monolayer sheet thickness of ~2 nm (Fig. S3). Furthermore, the synthesized $Ti_3C_2T_x$ MXene had abundant functional groups, such as –OH, –O, and –F, that were bonded to Ti atoms generated during the etching and delamination processes (Fig. S4). These functional groups enhanced the wettabilities of the MCNF electrodes in the aqueous electrolyte and the reaction solution[33]. The morphologies of the electrospun nanofibers (as-spun MXene/PAN mat, preoxidized MXene/PAN mat, and as-carbonized MCNF mat) are shown in Fig. S5. The bare MCNFs had smooth surfaces, and the MCNF fiber strands were intertwined, which preserved the electrode shape during the hydrothermal treatment. Images of the bare MCNFs showed that small MXene sheets were evenly distributed in the electrospun nanofibers, as we previously reported[20]. When fabricating the electrode, the amount of RuO_x formed was estimated by measuring the weight relative to that of the MCNFs (Fig. S6). The weight of the HT-MCNFs treated without the Ru precursor was reduced by 0.4%, indicating that the weight change of the MCNFs was negligible. The amount of RuO_x coated was increased by 12.8%, 19.0%, 29.9%, and 39.0% as the amount of Ru precursor relative to that of the MCNFs was increased 4-, 8-, 16-, and 32-fold (i.e., R4-MCNF, R8-MCNF, R16-MCNF, and R32-MCNF). The morphologies of HT-MCNFs and RuO_x-MCNFs as a function of the amount of Ru precursor used are shown in Fig. 2a–g and S7. The MXene sheets and TiO_2 formed on the surface of the HT-MCNF electrode are shown in Fig. 2a. When a small amount of RuO_x was added (R4-MCNF and R8-MCNF), the fiber surfaces were decorated (Fig. 2b, c, respectively). However, the use of additional Ru precursor during the hydrothermal process generated increasingly thick RuO_x coating layers (R16-MCNF and R32-MCNF; Fig. 2d, e, g, respectively). For example, the coating thickness of the R16-MCNFs was 55.2 nm (Fig. 2f), while the coating thickness of the R32-MCNFs was 86.5 nm (Fig. 2g). When an electrode was fabricated with a mass ratio of $RuCl_3 \cdot xH_2O$ to MCNF exceeding 32:1 (i.e., 48:1), the electrode was unstable and divided into several pieces containing short fiber fragments after the

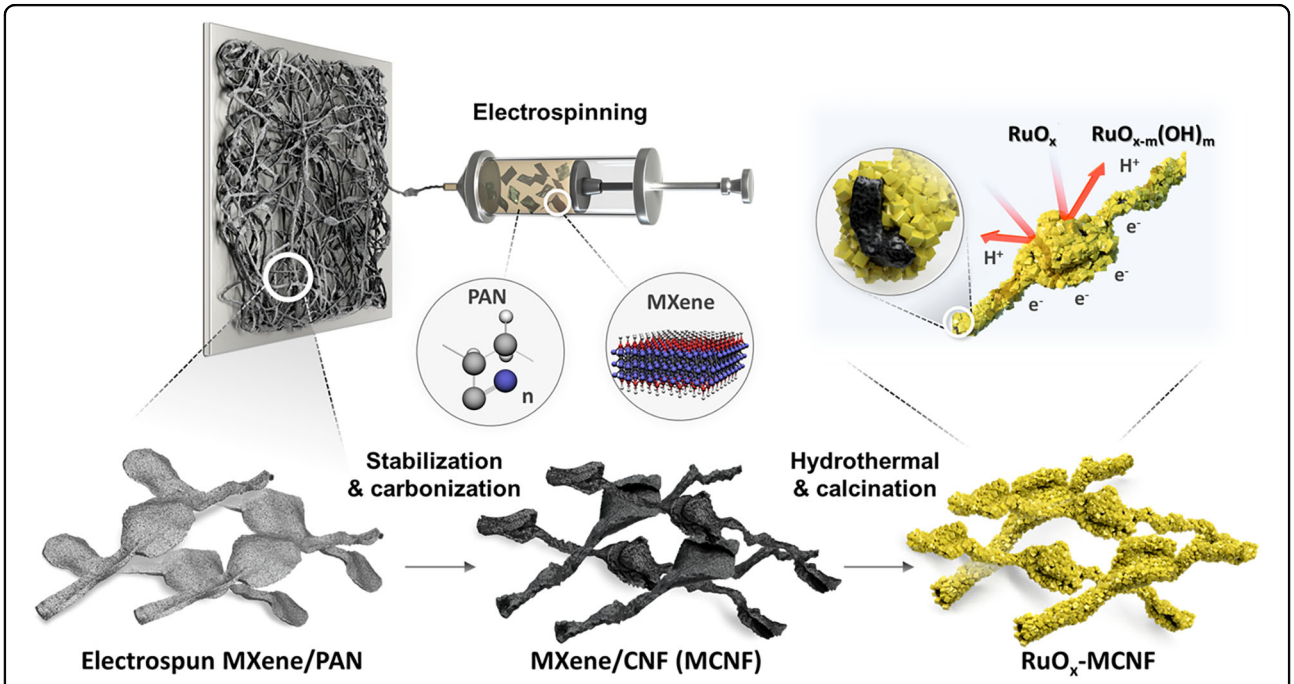

Fig. 1 Schematic illustration of the synthesis of RuO_x-coated $Ti_3C_2T_x$ MXene/carbon nanofiber (MCNF) electrodes. The electrospun MCNFs were immersed in an aqueous solution of $RuCl_3$ and hydrothermally treated.

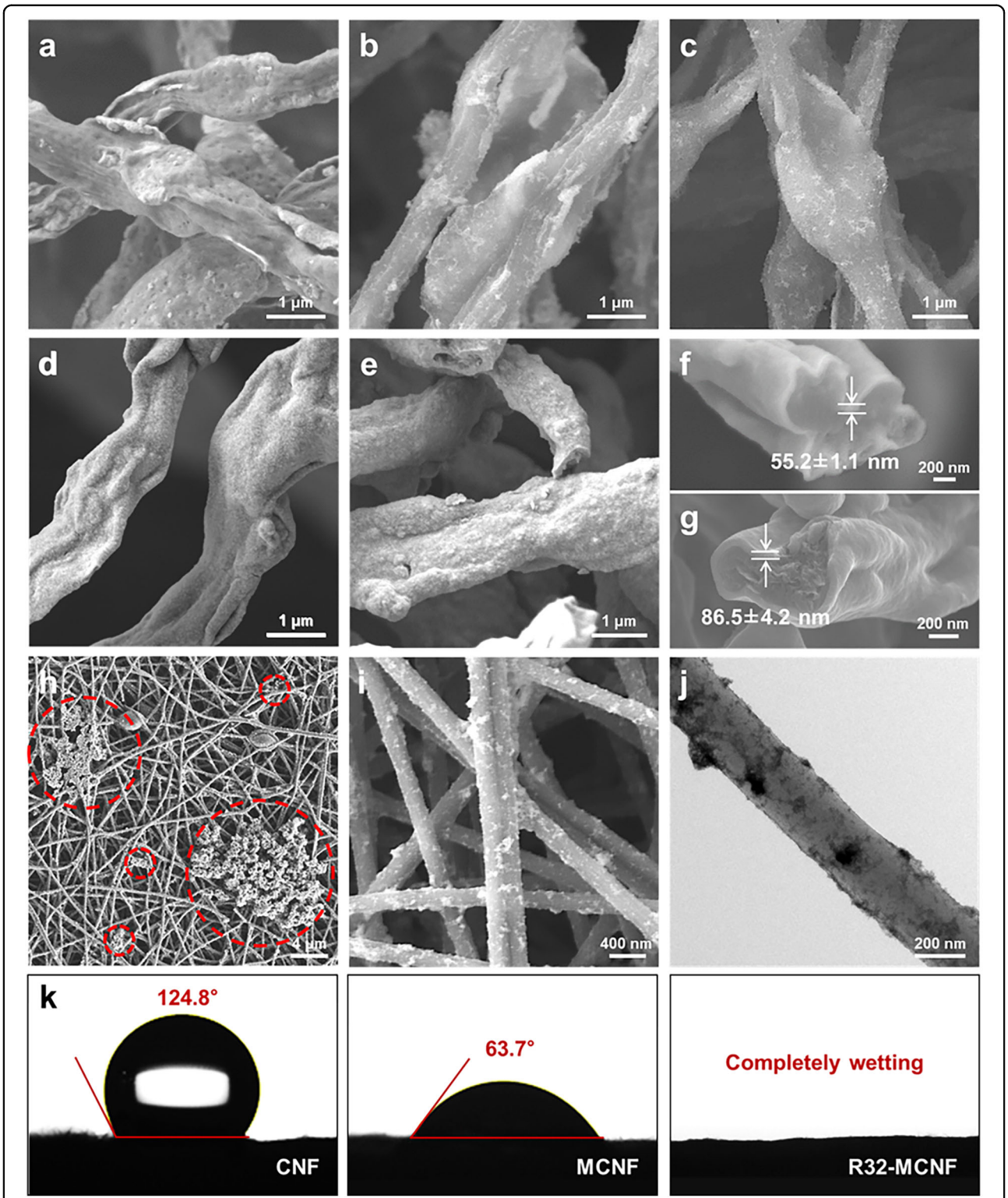

Fig. 2 Microstructure analyses and surface characterization. SEM images of the **a** HT-MCNFs; **b** R4-MCNFs; **c** R8-MCNFs; **d**, **f** R16-MCNFs; and **e**, **g** R32-MCNFs; **f**, **g** the thickness of the RuO_x coating layer. **h**, **i** SEM and **j** TEM images of the R32-CNF electrode. **k** Contact angles of the CNFs, MCNFs, and R32-MCNF electrodes measured after the water droplet rested for 180 s.

hydrothermal treatment (Fig. S9); it was clearly unsuitable for use as an electrode. The R32-MCNF composition contained the maximum RuO_x amount with which a stable shape was maintained. In addition, an R32-CNF electrode was prepared to compare the microstructures with/without MXene. The RuO_x appeared in the form of independent aggregated lumps with a high mass ratio of the Ru precursor (32-fold), as shown in Fig. 2h. The hydrophobic CNFs has fewer surface functional groups; thus, less RuO_x was formed along the surface during the hydrothermal reaction. The high-resolution SEM and TEM images (Fig. 2i, j) show that the RuO_x was not completely coated on the CNF surfaces but decorated. The water contact angles of the CNFs and MCNFs were also measured to confirm the effect of the MXene hydrophilicity on the surface properties of the CNFs (Fig. 2k). The contact angles of the CNFs with and without MXene were 63.7° and 124.8°, respectively, indicating the enhanced hydrophilicities of the CNFs resulting from the $Ti_3C_2T_x$ MXene surface functional groups. This helps to form the RuO_x evenly on the fibers during the hydrothermal process. As a result, it was confirmed that the $Ti_3C_2T_x$ MXene on the CNF surfaces served as a growth template for RuO_x due to the hydrophilic surface and functional groups.

X-ray diffraction was used to confirm the crystallinity and phase structure of the RuO_x (Fig. 3a). The R32-MCNF electrode displayed only TiO_2 peaks and no RuO_2 peaks, which indicated that the synthesized RuO_x had an amorphous structure. The TiO_2 rutile phase was formed by oxidation of the MXene in the electrode during the stabilization and carbonization processes; this phase was converted to the anatase phase during the hydrothermal treatment. The presence of RuO_x could not be confirmed by X-ray diffraction because of its amorphous nature. Thus, Raman and XPS analyses were used to obtain phase information. The Raman spectra of R32-MCNF, HT-MCNF, and commercial RuO_2 powder are presented in Fig. 3b. The commercial RuO_2 powder displayed three main peaks at 505, 620, and 683 cm^{-1} that were assigned to the E_g, A_{1g}, and B_{2g} vibrational modes of rutile RuO_2, respectively[34]. In contrast, the R32-MCNFs displayed two peaks at 496 and 612 cm^{-1}, which corresponded to the E_g and A_{1g} vibrational modes of rutile RuO_2. The two peaks for R32-MCNF were redshifted relative to the peaks of the commercial RuO_2 powder because of the disordered structure of the synthesized RuO_x[35,36] and the mechanical deformations generated by the phase difference between the oxygen-mediated chemically bonded MXenes and $RuOx$[37]. The chemical composition of the R32-MCNF surface was investigated with XPS (Fig. 3c). The XPS spectra contained peaks indicating the formation of RuO_x with Ru–O bonds and satellite peaks corresponding to the Ru 3d and Ru 3p binding energies. The binding energy of the main Ru $3d_{5/2}$ signal was 280.8 eV; the distance between the Ru $3d_{3/2}$ and Ru $3d_{5/2}$ doublets was 4.1 eV. These data were consistent with published values[38]. The Ru $3d_{5/2}$ satellite peak appeared at 282.0 eV because of interaction with another satellite peak at 286.2 eV. The Ru $3d_{3/2}$ signal intensity may be higher than that of the Ru $3d_{5/2}$ signal due to the presence of C from the CNFs (C–C 284.8 eV). The peaks at 529.3 and 530.8 eV in the O 1 s spectrum were assigned to Ru and O interactions and to O^{2-}/Ru–O bonds, respectively. The peak at 530.1 eV was attributed to Ru-O-Ti (Metal-O-Metal, M-O-M) bonds indicating oxygen-mediated chemical bonding between the MXenes and Ru ions[39]. The Ru-O-Ti peak was consistent with the results of the Raman analysis and convincingly demonstrated the formation of chemical bonds. In addition, the formation of these chemical bonds was also demonstrated by the peaks for Ti-O bonds in the O 1 s and Ti 2p XPS spectra. Finally, the peak at 532.7 eV was attributed to the oxygens in C–O species[40]. The crystallinity of the RuO_x coated on the MCNFs was investigated with transmission electron microscopy (Fig. 3d–f). The RuO_x was decorated on the surfaces of the MXene sheets protruding from the nanofibers in the image of the R8-MCNF electrode (Fig. 3d). The red-bordered region in Fig. 3e corresponded to the (110) plane of RuO_2 with an interplanar distance of 0.32 nm; some crystalline and amorphous regions were also apparent[41]. The yellow-bordered region in Fig. 3f indicated amorphous RuO_x and confirmed the absence of a regular atomic arrangement. The insets of Fig. 3e, f show the fast Fourier transform (FFT) patterns of the crystalline and amorphous regions, respectively, which suggested partially nanocrystalline RuO_x. Although some crystalline regions appeared to be present in RuO_x, we considered it to be completely amorphous because the crystalline portion was very small. The distribution of the RuO_x was also confirmed by elemental mapping using energy dispersive spectroscopy (Fig. S12).

The electrochemical utilities of the free-standing RuO_x-MCNF electrodes were characterized with the symmetric cell system in a 1 M H_2SO_4 aqueous solution. The effect of the RuO_x loading on the electrochemical performance was investigated in detail. Before complete electrochemical characterization, the potential window was optimized with CV experiments on the HT-MCNF electrode, which increased the maximum voltage at 50 mV/s from 0.6 to 1.0 V with a 0 V starting point (Fig. 13). Accordingly, the potential window was set at 0–0.7 V because the CV open tail did not appear with the MXene-added composite electrode. This finding was consistent with our previous results[20]. Electrochemical characterization was also used to study the calcination process occurring after the hydrothermal treatment. The observed XPS peaks corresponding to Ru–OH bonds in the

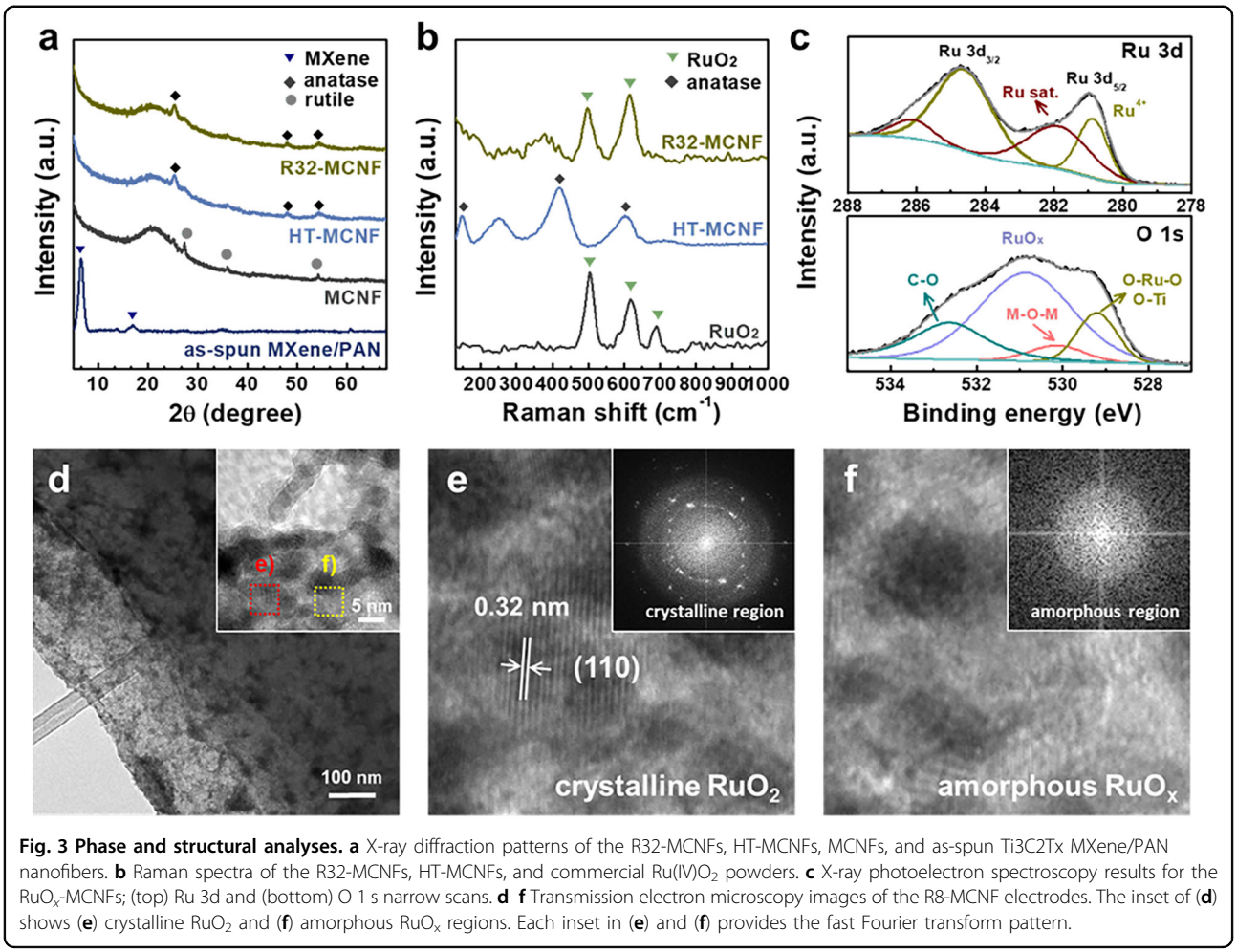

Fig. 3 Phase and structural analyses. a X-ray diffraction patterns of the R32-MCNFs, HT-MCNFs, MCNFs, and as-spun Ti3C2Tx MXene/PAN nanofibers. **b** Raman spectra of the R32-MCNFs, HT-MCNFs, and commercial Ru(IV)O_2 powders. **c** X-ray photoelectron spectroscopy results for the RuO_x-MCNFs; (top) Ru 3d and (bottom) O 1 s narrow scans. **d**–**f** Transmission electron microscopy images of the R8-MCNF electrodes. The inset of (**d**) shows (**e**) crystalline RuO_2 and (**f**) amorphous RuO_x regions. Each inset in (**e**) and (**f**) provides the fast Fourier transform pattern.

uncalcined RuO_x/OH-MCNF electrode were consistent with incomplete formation of the RuO_x (Fig. 14); they would likely affect the electrochemical performance. Figure S15 shows that the CV curves of both samples were similar at a low scan rate of 2 mV/s; however, at a high scan rate of 300 mV/s, the RuO_x/OH-MCNF electrode showed a much worse performance than the RuO_x-MCNF electrode. In addition, Nyquist plots confirmed that the electrode resistance and charge transfer resistance were much lower for the RuO_x-MCNFs than for the RuO_x/OH-MCNFs (Fig. S16). Therefore, calcination of the electrode after the hydrothermal treatment enhanced its electrochemical performance. The CV curves of the RuO_x-MCNF electrodes generated at a slow scan rate of 2 mV/s (Fig. 4a) and a fast scan rate of 300 mV/s (Fig. 4b) exhibited almost rectangular shapes, which is typical pseudocapacitive behavior for RuO_2[42]. These results indicated good capacitive behavior with fast charging/discharging rates. The difference in specific currents between the electrodes reflected the change in capacity due to the amount of RuO_x added. The RuO_x-MCNF electrodes had larger integrated CV areas than the HT-MCNFs synthesized without the Ru precursor, which suggested high capacitance related to the pseudocapacitive nature of RuO_x. The R32-MCNF electrode had the optimal integrated area for all scan rates, indicating good capacitance and high electrochemical reversibility. Therefore, as long as the MCNF electrode could withstand the Ru precursor solution (i.e., remain in one piece), the electrochemical performance improved as the amount of RuO_x coating increased. Figure S17 presents GCD curves for HT-MCNF and all of the RuO_x-MCNF electrodes at low and high current densities. As with the CV results, when RuO_x was coated on the surface, the charging/discharging times increased, and symmetric behavior was observed. Figure 4c shows a plot of the specific capacitance as a function of scan rate from 2 to 300 mV/s. The capacitance was increased with increasing RuO_x content; the R32-MCNF electrode showed the highest capacitance of 279.4 F/g at a scan rate of 2 mV/s. This result was 2.6-fold higher than the capacitance of the HT-MCNFs (106.1 F/g) at the same scan rate; these trends

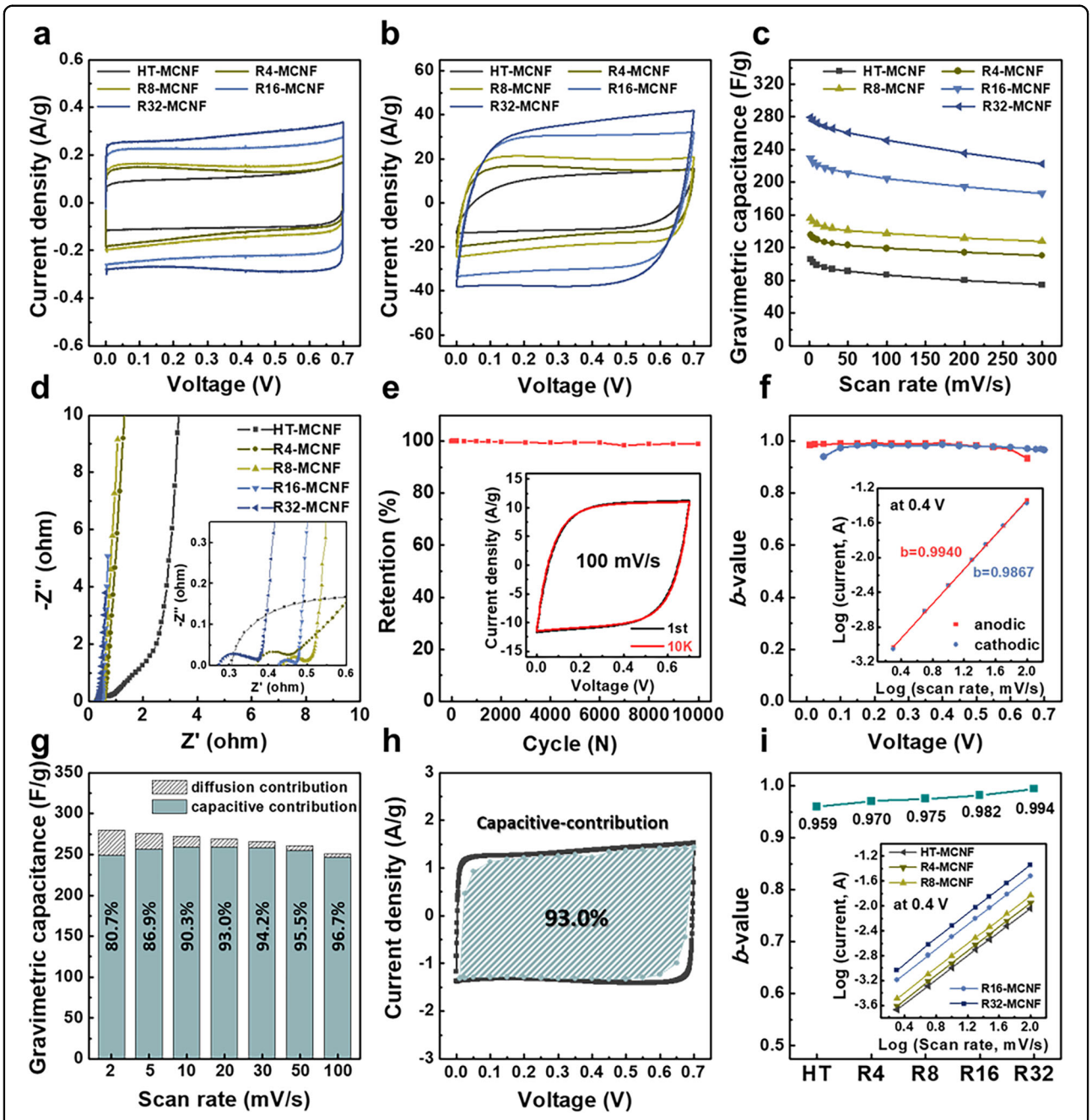

Fig. 4 Electrochemical data for the HT-MCNF and RuO_x-MCNF electrodes. a Cyclic voltammetry (CV) curves measured at scan rates of (**a**) 2 and (**b**) 300 mV/s. **c** Variations in the gravimetric capacitance as a function of the scan rate. **d** Nyquist plots for all electrodes. **e** Cycling stability of the R32-MCNF electrode during 10,000 CV tests. f–**i** Charge-storage mechanism of RuO_x-MCNF electrodes for capacitive contribution analysis. **f** *b*-Values of the R32-MCNF electrode at various voltages. The inset of (**f**) shows the current response as a function of scan rate at 0.4 V. **g** Contribution ratio of the capacitance of the R32-MCNF electrode at different scan rates. **h** Capacitive contribution to charge storage at a scan rate of 20 mV/s with CV curves for the R32-MCNF electrode. **i** *b*-values and current responses of all electrodes.

were consistent with the CV results. All of the RuO_x-MCNF electrodes displayed very high-rate capabilities, with retention rates exceeding 80% as the scan rate was increased from 2 to 300 mV/s. These high rates were attributed to the ionic conductivity of the RuO_x and the electrical conductivity of the $Ti_3C_2T_x$ MXene[20]. The open framework and fast ion diffusion were also beneficial[43]. EIS measurements were performed to examine the electrolyte kinetics and improved conductivity of the composite electrodes; the resulting Nyquist plots are shown in

Fig. 4d. The electrode resistance (R_d), which is the contact resistance between the electrolyte and electrode surface in the high-frequency region, was lowest (0.28 Ω) for R32-MCNF among the RuO_x-MCNF and HT-MCNF electrodes. The charge transfer resistance of R32-MCNF (0.078 Ω) was smaller than that of HT-MCNF (0.40 Ω). Furthermore, the ionic conductivities (σ_{ion}) of all samples were calculated with the equation $\sigma_{ion} = L/(R_{ct}\ A)$, where L and A are the thickness and area of an electrode, respectively. Similar to the R_{ct} trend, all of the RuO_x-MCNF electrodes exhibited significantly higher ionic conductivities than the HT-MCNFs (Table S1).

This result was also supported by the contact angles of the electrodes (Fig. 2k). The wettability with the aqueous electrolyte was improved by the formation of the RuO_x coating layer, and the enhanced wettability facilitated fast charge transport. The EIS spectra for the R32-MCNFs were fitted with the Randles circuit (Fig. S18); the calculated resistances are provided in Table S1. Figure 4e and S19 present the cycling data measured at 100 mV/s for all of the electrodes. The capacitance decrease of the R32-MCNF electrode (Fig. 4e) was negligible, with 98.9% capacitance retention after 10 K cycles; the shape of the CV curve (inset) was unchanged between cycles 1 and 10 K, demonstrating stable device operation. The cycle stability results for all electrodes are presented in Fig. S19; all of the RuO_x-MCNF electrodes showed greater stability after 5000 (5 K) cycles than the HT-MCNF electrode (i.e., 92.2% for HT-MCNF, 95.4% for R4-MCNF, 94.5% for R8-MCNF, 96.8% for R16-MCNF, and 99.4% for R32-MCNF). These results were related to the amorphous structure of the RuO_x; the strain and stress were isotropic during charging/discharging, which enhanced the long-term stability. Therefore, structural distortions or mechanical strain due to the redox reactions could be accommodated in a more efficient manner, which extended the cycle life[44,45]. A uniform and thick coating of RuO_x provided the best cycle stability, as demonstrated by the results for the R32-MCNF electrode. The shape of the R48-MCNF electrode, which contained more Ru precursor than did the R32-MCNF electrode, collapsed because it was unable to maintain its structure; the electrochemical performance decreased slightly. The CV and GCD curves presented in Fig. S20 indicated stability, but the capacitance of 254.3 F/g measured at a scan rate of 2 mV/s was slightly lower than the capacitance of the R32-MCNF electrode. In addition, the capacitance retention rate at 300 mV/s was only 74.9%. An EIS analysis confirmed that both the electrode resistance and charge transfer resistance increased; these findings were attributed to poor contact because of the structural instability. The cycling stability was 98.8% after 5 K cycles and 98.6% after 10 K cycles; these values were better than those of the HT-MCNF and other RuO_x-MCNF electrodes but worse than that of the R32-MCNF electrode. The fragmented R48-MCNF electrode did not maintain its shape and displayed reduced electrochemical performance, thus confirming that the R32-MCNF electrode was the optimal design.

The diffusion-controlled and capacitive-controlled (surface reaction) contributions of the total specific capacitance were analyzed to investigate the charge storage and rate-dependent kinetics of the R32-MCNF electrode[46]. For this analysis, CV experiments were conducted at scan rates of 2, 5, 10, 20, 30, 50, and 100 mV/s. The measured i_{total} consists of the slow diffusion-controlled process (i_d) and the capacitive-controlled process (i_c), which are defined as follows:

$$i_{total} = i_d + i_c = a\nu^b \tag{5}$$

$$\log i = \log a + b \log \nu \tag{6}$$

where ν is the scan rate and a and b are variable parameters. The b-value is obtained from the slope of a plot of log$i$ versus logν. Ideally, the b-value is 0.5 for a diffusion-controlled contribution and 1 for a capacitive-controlled contribution (surface reaction). As illustrated in Fig. 4f, the b-values for the anodic and cathodic current peaks seen at various voltages were in the range of 0.93–0.99, excluding the terminal voltage, which indicated a dominant capacitive contribution. The inset of Fig. 4f shows the current response as a function of scan rate at a 0.4 V voltage for the R32-MCNF electrode; the slopes of the plots corresponded to the b-values. The following equations were used to analyze the capacitive- and diffusion-limited contributions quantitatively:

$$i(V) = k_1\nu + k_2\nu^{\frac{1}{2}} \tag{7}$$

$$\frac{i(V)}{\nu^{\frac{1}{2}}} = k_1\nu^{\frac{1}{2}} + k_2 \tag{8}$$

where $i(V)$ is the current at a fixed potential, $k_1\nu$ is the capacitive-controlled current, and $k_2\nu^{\frac{1}{2}}$ is the diffusion-controlled current. The calculated ratios of these currents and the adapted CV partition curves are illustrated in Fig. 4g, h. The capacitive contribution of the R32-MCNF electrode increased from 80.7% at a scan rate of 2 mV/s to 96.7% at a scan rate of 100 mV/s (Fig. 4g); the CV curve showing the contribution ratio at a scan rate of 20 mV/s was in good agreement (Fig. 4h). These results, even at the high scan rate of 100 mV/s, indicated enhanced rate performance and durability (i.e., faster electron transfer and excellent cycling stability)[47]. Figure 4i shows the current responses of the anodic peak at 0.4 V for all electrodes, along with the b-values calculated from the slopes (inset). The b-value increased from that of the HT-

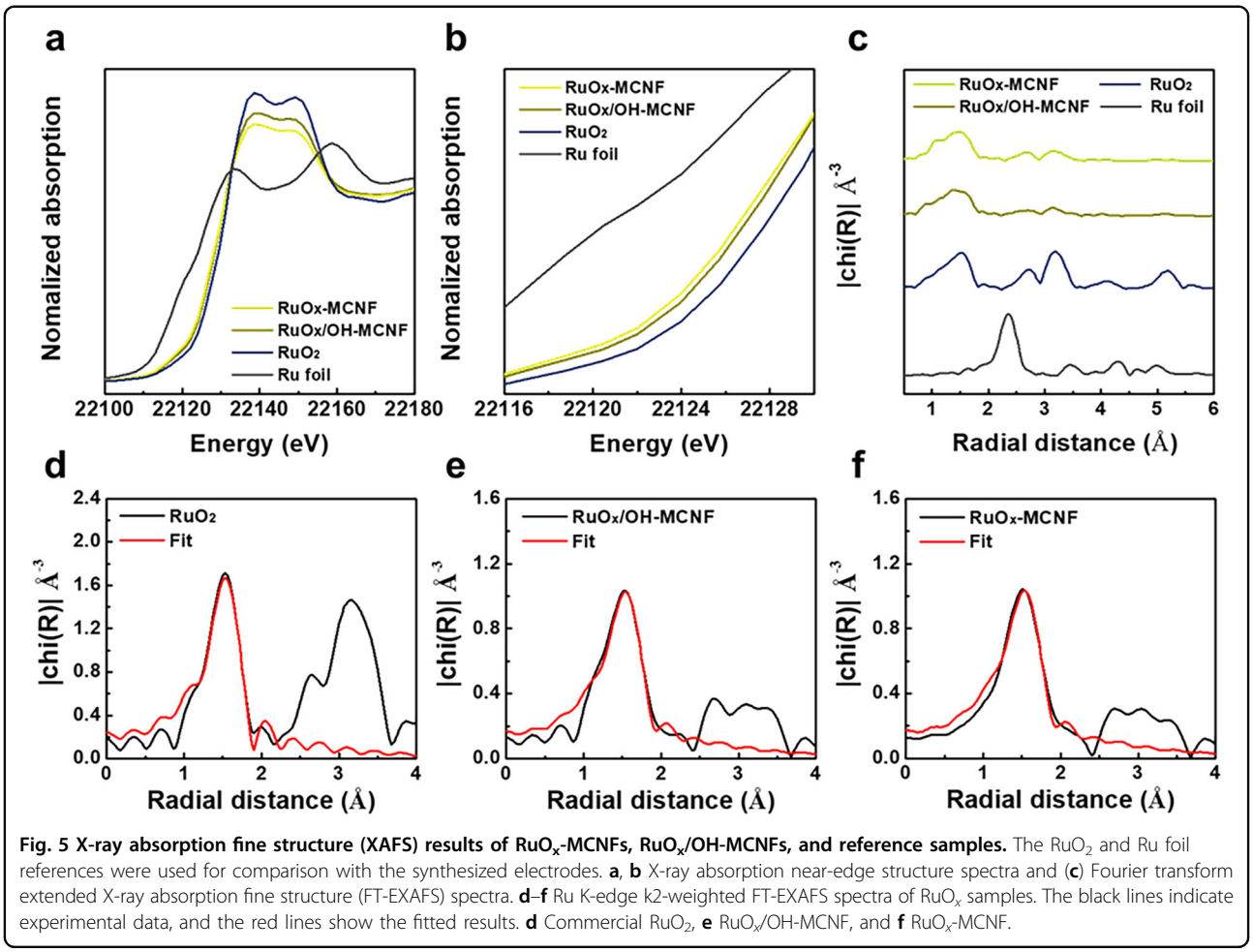

Fig. 5 X-ray absorption fine structure (XAFS) results of RuO_x-MCNFs, RuO_x/OH-MCNFs, and reference samples. The RuO_2 and Ru foil references were used for comparison with the synthesized electrodes. **a**, **b** X-ray absorption near-edge structure spectra and (**c**) Fourier transform extended X-ray absorption fine structure (FT-EXAFS) spectra. **d**–**f** Ru K-edge k2-weighted FT-EXAFS spectra of RuO_x samples. The black lines indicate experimental data, and the red lines show the fitted results. **d** Commercial RuO_2, **e** RuO_x/OH-MCNF, and **f** RuO_x-MCNF.

MCNF electrode as the amount of RuO_x was increased. This indicated capacitive-controlled behavior that enabled the fast current responses of the supercapacitors.

The electronic structures and local coordination environments of the RuO_x samples were analyzed by XAS to relate the oxidation states and degrees of disorder to the enhanced electrochemical performance of the RuO_x-containing electrodes. X-ray absorption near-edge structure analyses revealed electronic structure differences among the RuO_x-containing samples (Fig. 5a, b). The absorption edge was shifted to lower energy for Ru metal relative to that for RuO_2 because of the lower oxidation state of the metal. The absorption edge energies of RuO_x/OH-MCNF and RuO_x-MCNF were slightly lower than the absorption edge energy of RuO_2, which indicated that the Ru in both samples had a slightly lower oxidation state than that in RuO_2. This result supported the notion that the various oxidation states of the RuO_x electrodes assist charge transport[48]. Extended X-ray absorption fine structure (EXAFS) spectra were used to analyze the chemical structures of the RuO_x samples (Fig. 5c). The primary peak observed at 2.36 Å for metallic Ru foil was assigned to Ru–Ru interactions, while the commercial RuO_2 displayed peaks at 1.51, 2.73, and 3.19 Å. The peak at 1.51 Å was associated with the scattering path of Ru-O with the first nearest neighbor O atoms, while the peaks at 2.73 and 3.19 Å arose from Ru–Ru scattering paths in the second and the third shells[49]. An EXAFS fitting analysis was then used to reveal differences in the local coordination environments of the RuO_x/OH-MCNFs, RuO_x-MCNFs, and RuO_2 (Fig. 5d–f and Table S2). The RuO_x/OH-MCNF and RuO_x-MCNF samples displayed lower peak intensities for the first coordination shell (Ru–O) than RuO_2, which could indicate a lower coordination number and/or higher structural disorder in the local coordination environment. Fitting of the first coordination shells revealed that both the RuO_x/OH-MCNF and RuO_x-MCNF samples had low coordination numbers: 5.3 ± 0.8 and 5.8 ± 0.9, respectively. The mean Ru–O bond lengths were longer for RuO_x/OH-MCNF and RuO_x-MCNF (1.99 ± 0.1 Å) than for RuO_2, which has two Ru–O bonds with lengths of 1.95 ± 0.1 Å and four Ru–O bonds with lengths of 1.99 ± 0.1 Å. The slightly reduced oxidation states of the RuO_x/OH-MCNFs and RuO_x-MCNFs indicated by the X-ray absorption near-

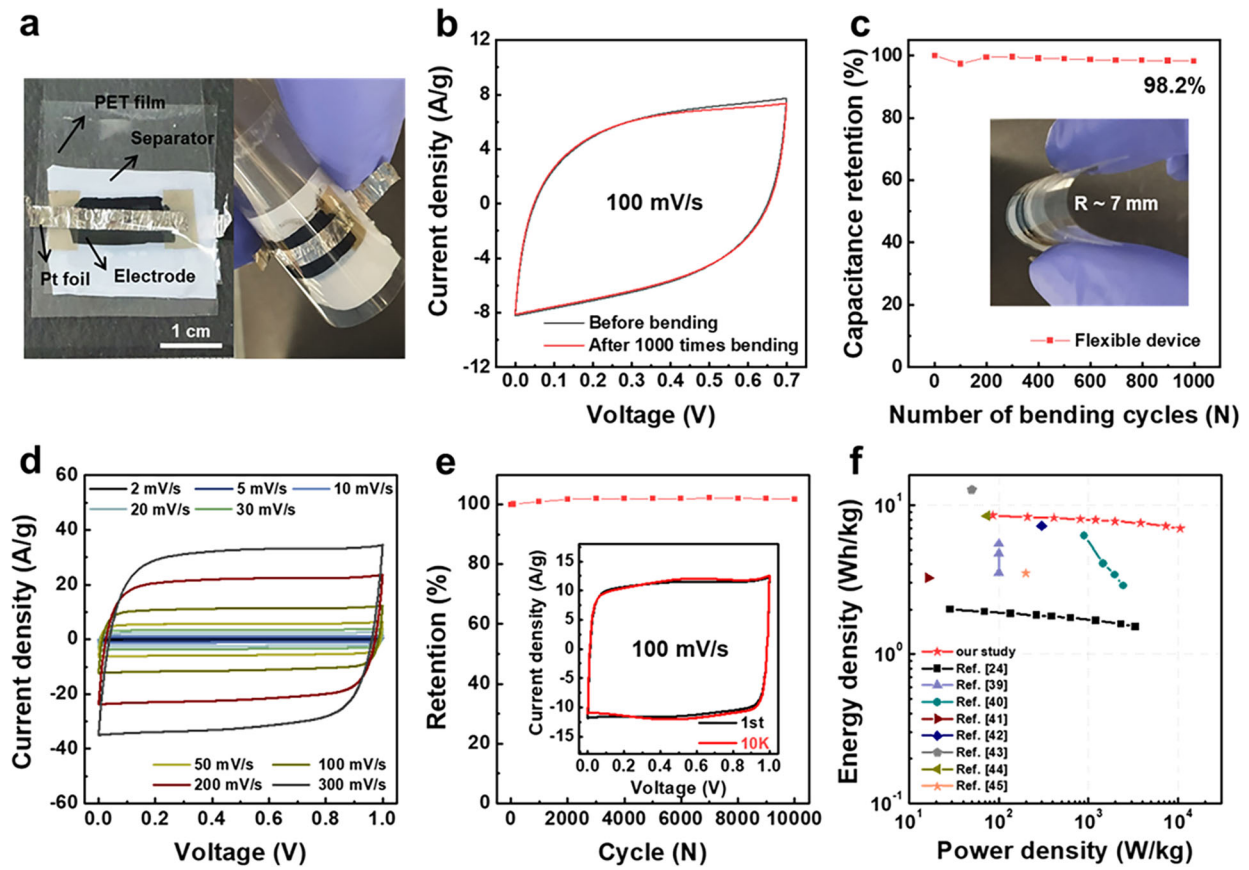

Fig. 6 Flexible device characterization and electrochemical data in widen voltage window for RuOx-MCNF electrodes. a–c A flexible MCNF-based electrode device. **a** Digital photograph of a flexible device prototype. **b** CV curves measured at scan rates of 100 mV/s before and after 1000 bending cycles and **c** capacitance retention of the device versus the number of bending cycles. The bending radius was ~7 mm. **d–f** Electrochemical performance of the R32-MCNF electrode over a wide voltage window of 1.0 V. **d** CV curves measured at different scan rates, **e** cycling stability at a scan rate of 100 mV/s, and **f** Ragone plots for the electrodes synthesized in this work. The energy and power densities were calculated based on the total masses of the electrodes.

edge structure analyses were also explained by the lower coordination numbers and longer bond lengths for Ru with the nearest coordinating O. The Debye–Waller factor (σ^2) describes the structural disorder of a given path; the value of 0.005 ± 0.001 for the RuO_x/OH-MCNFs and RuO_x-MCNFs was much higher than the value for RuO_2 (0.001 ± 0.002). Thus, the structural disorder was significantly higher in the RuO_x/OH-MCNFs and RuO_x-MCNFs than in RuO_2. This disorder facilitated transport by shortening the charge-transfer paths, which led to the improved electrochemical performance[44].

To investigate the potential for application as robust electrodes in flexile supercapacitors, a prototype flexible device was fabricated by using two pieces of R32-MCNF. Similar to the electrolyte (i.e., H_2SO_4) contained in the devices using liquid electrolytes, a PVA-H_2SO_4 gel was used as the electrolyte in the flexible device, as shown in Fig. 6a. A plot of the gravimetric capacitance versus the scan rate is shown in Fig. S21. The capacitance values of polymer gel electrolyte systems were generally lower than those of the liquid-based electrolytes. Our flexible device showed the same trends, but surprisingly, our R32-MCNF-based flexible device exhibited a high specific capacitance of 175.7 F/g at 2 mV/s and still maintained a capacitance of 147.4 F/g even at a fast scan rate of 300 mV/s. Furthermore, the superior mechanical flexibility of the MCNFs provided the same mechanical robustness of the RuO_x-MCNFs composite electrodes, and hence, the CV curve for the flexible device showed an almost identical shape as the flat electrode even after 1000 bending cycles (Fig. 6b). In this repeated bending test, the bending radius was ~7 mm, and the flexible device retained ~98.2% of its initial capacitance (Fig. 6c). Therefore, the RuO_x-MCNF-based electrode has great potential for use in both conventional and flexible supercapacitors.

The electrochemical performance was also assessed by increasing the voltage window for the R32-MCNF

electrode to 1.0 V to achieve a higher energy density (Fig. 6d–f). Although the MCNF electrode was restricted to a voltage range below 0.7 V because of the $Ti_3C_2T_x$ MXene, the R32-MCNF electrode with RuO_x completely covering the surface was studied up to 1.0 V in the H_2SO_4 electrolyte system[20]. The CV curves exhibited stable rectangular shapes at various scan rates, even at a fast scan rate of 300 mV/s; the cycling stability did not reveal any reduction in capacitance even after 10 K CV cycles. Figure 6f shows Ragone plots used to illustrate the gravimetric energies and power densities. The R32-MCNF electrode exhibited a maximum energy density of 8.5 Wh/kg with a power density of 85.8 W/kg; these values were 4.25-time higher than the values of a previously reported MCNF electrode[20,50–56]. Considering that the binder-free and free-standing electrodes were studied in a two-electrode symmetric cell system, these values were very high. In addition, to compare the capacitance values of the electrodes manufactured in this study with those reported previously, the specific capacitances from the previous studies are shown in Table S3. The RuO_x-MCNF electrodes prepared in this study displayed the highest capacitance; stable high-rate performance was achieved because the capacitance reduction rates were very low even at high scan rates.

Conclusion

We developed free-standing RuO_x-coated $Ti_3C_2T_x$ MCNF electrodes with various RuO_x contents by using a facile and efficient electrospinning and hydrothermal method. The RuO_x-MCNF electrodes exhibited high gravimetric capacitances up to 279.4 F/g at a slow scan rate of 2 mV/s; they maintained a high capacitance retention rate of 80% (222.5 F/g) at a scan rate of 300 mV/s, which demonstrated excellent rate performance. They also displayed long-term cycling stability with 99% retention after 10 K charge/discharge cycles. This enhanced electrochemical performance was attributed to the presence of numerous channels allowing passage of the electrolyte ions through RuO_x. The RuO_x prepared in this study was almost amorphous and formed an optimal coating layer; this made it possible to significantly improve the electrochemical performance while maintaining the CNF morphology. Moreover, the addition of the conductive $Ti_3C_2T_x$ MXene improved the electrochemical performance while maintaining the hydrophilicities of the fiber electrodes, which enabled the formation of a uniform RuO_x coating layer during the hydrothermal treatment. Introduction of the third component (i.e., RuO_x) and optimization of the physical properties (coating amount, crystallinity control, and heat treatment) are very important for the fiber-based electrodes. The results reported herein support the use of RuO_x and its electrospun composite electrodes in high electrochemical performance flexible energy storage systems.

Acknowledgements

This work was supported by a National Research Foundation of Korea (NRF) grant funded by the Korean government (Ministry of Science and ICT) (2021R1F1A1058854) and a National Research Council of Science & Technology (NST) grant by the Korean government (MSIT) (No. CAP22071-000). Experiments at PLS-II were supported in part by MSIT and POSTECH.

Author details

[1]Department of Urban, Energy, and Environmental Engineering, Chungbuk National University, Chungdae-ro 1, Seowon-Gu, Cheongju, Chungbuk 28644, Republic of Korea. [2]Center for Energy Materials Research, Korea Institute of Science and Technology (KIST), 5, Hwarang-ro 14-gil, Seongbuk-gu, Seoul 02792, Republic of Korea. [3]Pohang Accelerator Laboratory, 80 Jigokro-123-beongil, Nam-gu, Pohang 37673 Gyeongbuk, Republic of Korea. [4]High Temperature Energy Conversion Laboratory, Korea Institute of Energy Research (KIER), 152 Gajeong-ro, Yuseong-gu, Daejeon 34129, Republic of Korea. [5]Department of Advanced Materials Engineering, Chungbuk National University, Chungdae-ro 1, Seowon-Gu, Cheongju, Chungbuk 28644, Republic of Korea

Author contributions

All authors contributed extensively to the work presented in this paper. H.H., S.B., and D.L. designed the experiment. S.B. and D.L. supervised the work. H.H. and S.Y. prepared the samples. H.H., S.Y., and K.L. measured the microstructures, physical properties and electrochemical performance. H.H. and S.Y. analyzed the data. H.H., S.B., and D.L. prepared the original draft. All authors reviewed and edited the manuscript. All authors have read and agreed to the published version of the manuscript.

Competing interests

The authors declare no competing interests.

Publisher's note

Springer Nature remains neutral with regard to jurisdictional claims in published maps and institutional affiliations.

Supplementary information The online version contains supplementary material available at https://doi.org/10.1038/s41427-023-00476-x.

Received: 1 November 2022 Revised: 15 March 2023 Accepted: 20 March 2023.
Published online: 12 May 2023

References

1. Simon, P. & Gogotsi, Y. Materials for electrochemical capacitors. *Nat. Mater.* **7**, 845–854 (2008).
2. Chen, D., Jiang, K., Huang, T. & Shen, G. Recent advances in fiber supercapacitors: materials, device configurations, and applications. *Adv. Mater.* **32**, 1901806 (2020).
3. Choi, H.-J. et al. Graphene for energy conversion and storage in fuel cells and supercapacitors. *Nano Energy* **1**, 534–551 (2012).
4. Lang, J. et al. Highly enhanced energy density of supercapacitors at extremely low temperatures. *J. Power Sources* **423**, 271–279 (2019).
5. Zhu, Q., Li, J., Simon, P. & Xu, B. Two-dimensional MXenes for electrochemical capacitor applications: progress, challenges and perspectives. *Energy Storage Mater.* **35**, 630–660 (2021).
6. Snook, G. A., Kao, P. & Best, A. S. Conducting-polymer-based supercapacitor devices and electrodes. *J. Power Sources* **196**, 1–12 (2011).
7. An, C., Zhang, Y., Guo, H. & Wang, Y. Metal oxide-based supercapacitors: progress and prospectives. *Nanoscale Adv.* **1**, 4644–4658 (2019).
8. Lang, X., Hirata, A., Fujita, T. & Chen, M. Nanoporous metal/oxide hybrid electrodes for electrochemical supercapacitors. *Nat. Nanotechnol.* **6**, 232–236 (2011).

9. Wang, G., Zhang, L. & Zhang, J. A review of electrode materials for electrochemical supercapacitors. *Chem. Soc. Rev.* **41**, 797–828 (2012).
10. Hu, M. et al. Emerging 2D MXenes for supercapacitors: status, challenges and prospects. *Chem. Soc. Rev.* **49**, 6666–6693 (2020).
11. Rani, J. R., Thangavel, R., Kim, M., Lee, Y. S. & Jang, J. H. Ultra-high energy density hybrid supercapacitors using $MnO_{(2)}$/reduced graphene oxide hybrid nanoscrolls. *Nanomaterials* **10**, 2049 (2020).
12. Mozaffari, S. A., Mahmoudi Najafi, S. H. & Norouzi, Z. Hierarchical NiO@Ni(OH)$_2$ nanoarrays as high-performance supercapacitor electrode material. *Electrochim. Acta* **368**, 137633 (2021).
13. Jiang, Q., Kurra, N., Alhabeb, M., Gogotsi, Y. & Alshareef, H. N. All pseudocapacitive MXene-RuO_2 asymmetric supercapacitors. *Adv. Energy Mater.* **8**, 1703043 (2018).
14. Wang, Y. et al. Recent progress in carbon-based materials for supercapacitor electrodes: a review. *J. Mater. Sci.* **56**, 173–200 (2021).
15. Dong, D. Ternary composite MnO_2@MoS_2/polypyrrole from in-situ synthesis for binder-free and flexible supercapacitor. *J. Bioresour. Bioprod.* **4**, 242–250 (2019).
16. Hu, L. et al. Symmetrical MnO_2–carbon nanotube–textile nanostructures for wearable pseudocapacitors with high mass loading. *ACS Nano* **5**, 8904–8913 (2011).
17. Li, H., Li, X., Liang, J. & Chen, Y. Hydrous RuO_2-decorated MXene coordinating with silver nanowire inks enabling fully printed micro-supercapacitors with extraordinary volumetric performance. *Adv. Energy Mater.* **9**, 1803987 (2019).
18. Xiao, X. et al. Freestanding mesoporous VN/CNT hybrid electrodes for flexible all-solid-state supercapacitors. *Adv. Mater.* **25**, 5091–5097 (2013).
19. Yuan, L. et al. Flexible solid-state supercapacitors based on carbon nanoparticles/MnO_2 nanorods hybrid structure. *ACS Nano* **6**, 656–661 (2012).
20. Hwang, H. et al. High-rate electrospun $Ti_3C_2T_x$ MXene/carbon nanofiber electrodes for flexible supercapacitors. *Appl. Surf. Sci.* **556**, 149710 (2021).
21. Kebabsa, L., Kim, J., Lee, D. & Lee, B. Highly porous cobalt oxide-decorated carbon nanofibers fabricated from starch as free-standing electrodes for supercapacitors. *Appl. Surf. Sci.* **511**, 145313 (2020).
22. Feng, S. et al. One-step synthesis of carbon nanosheet-decorated carbon nanofibers as a 3D interconnected porous carbon scaffold for lithium–sulfur batteries. *J. Mater. Chem. A* **5**, 23737–23743 (2017).
23. Lu, F., Wang, J., Sun, X. & Chang, Z. 3D hierarchical carbon nanofibers/TiO_2@MoS_2 core-shell heterostructures by electrospinning, hydrothermal and in-situ growth for flexible electrode materials. *Mater. Des.* **189**, 108503 (2020).
24. Lai, F., Huang, Y., Miao, Y.-E. & Liu, T. Controllable preparation of multi-dimensional hybrid materials of nickel-cobalt layered double hydroxide nanorods/nanosheets on electrospun carbon nanofibers for high-performance supercapacitors. *Electrochim. Acta* **174**, 456–463 (2015).
25. Naguib, M. et al. Two-dimensional nanocrystals produced by exfoliation of Ti_3AlC_2. *Adv. Mater.* **23**, 4248–4253 (2011).
26. Lukatskaya, M. R. et al. Cation intercalation and high volumetric capacitance of two-dimensional titanium carbide. *Science* **341**, 1502–1505 (2013).
27. Han, Z. J. et al. RuO_2-coated vertical graphene hybrid electrodes for high-performance solid-state supercapacitors. *J. Mater. Chem. A* **5**, 17293–17301 (2017).
28. Hwang, J. Y. et al. Direct preparation and processing of graphene/RuO_2 nanocomposite electrodes for high-performance capacitive energy storage. *Nano Energy* **18**, 57–70 (2015).
29. Wu, X. et al. High-rate supercapacitor utilizing hydrous ruthenium dioxide nanotubes. *J. Power Sources* **294**, 88–93 (2015).
30. Zheng, J. P., Cygan, P. J. & Jow, T. R. Hydrous ruthenium oxide as an electrode material for electrochemical capacitors. *J. Electrochem. Soc.* **142**, 2699–2703 (1995).
31. Gujar, T. P. et al. Spray deposited amorphous RuO_2 for an effective use in electrochemical supercapacitor. *Electrochem. Commun.* **9**, 504–510 (2007).
32. Zhou, Z. et al. Amorphous RuO_2 coated on carbon spheres as excellent electrode materials for supercapacitors. *RSC Adv.* **4**, 6927–6932 (2014).
33. Alhabeb, M. et al. Guidelines for synthesis and processing of two-dimensional titanium carbide ($Ti_3C_2T_x$ MXene). *Chem. Mater.* **29**, 7633–7644 (2017).
34. Tsuji, E., Imanishi, A., Fukui, K.-I. & Nakato, Y. Electrocatalytic activity of amorphous RuO_2 electrode for oxygen evolution in an aqueous solution. *Electrochim. Acta* **56**, 2009–2016 (2011).
35. Meng, L.-J., Teixeira, V. & dos Santos, M. P. Raman spectroscopy analysis of magnetron sputtered RuO_2 thin films. *Thin Solid Films* **442**, 93–97 (2003).
36. Mar, S. Y., Chen, C. S., Huang, Y. S. & Tiong, K. K. Characterization of RuO_2 thin films by Raman spectroscopy. *Appl. Surf. Sci.* **90**, 497–504 (1995).
37. Shi, J. et al. Ru-Ti oxide based catalysts for HCl oxidation: the favorable oxygen species and influence of Ce additive. *Catalysts* **9**, 108 (2019).
38. Kwak, K.-H., Kim, D. W., Kang, Y. & Suk, J. Hierarchical Ru- and RuO_2-foams as high performance electrocatalysts for rechargeable lithium–oxygen batteries. *J. Mater. Chem. A* **4**, 16356–16367 (2016).
39. Zhao, S. et al. The diffusion of low-energy methyl group on ITO film surface and its impact on optical-electrical properties. *Materials* **11**, 1991 (2018).
40. Cox, P. A., Goodenough, J. B., Tavener, P. J., Telles, D. & Egdell, R. G. The electronic structure of $Bi_{2-x}Gd_xRu_2O_7$ and RuO_2: a study by electron spectroscopy. *J. Solid State Chem.* **62**, 360–370 (1986).
41. Kim, S.-j et al. Highly branched RuO_2 nanoneedles on electrospun TiO_2 nanofibers as an efficient electrocatalytic platform. *ACS Appl. Mater. Interfaces* **7**, 15321–15330 (2015).
42. Liu, C. et al. Scalable, binderless, and carbonless hierarchical Ni nanodendrite foam decorated with hydrous ruthenium dioxide for 1.6 V symmetric supercapacitors. *Adv. Mater. Interfaces* **3**, 1500503 (2016).
43. Liang, M., Zhao, M., Wang, H., Zheng, Q. & Song, X. Superior cycling stability of a crystalline/amorphous Co_3S_4 core–shell heterostructure for aqueous hybrid supercapacitors. *J. Mater. Chem. A* **6**, 21350–21359 (2018).
44. Li, H. B. et al. Amorphous nickel hydroxide nanospheres with ultrahigh capacitance and energy density as electrochemical pseudocapacitor materials. *Nat. Commun.* **4**, 1894 (2013).
45. Chen, J., Xu, J., Zhou, S., Zhao, N. & Wong, C.-P. Amorphous nanostructured FeOOH and Co–Ni double hydroxides for high-performance aqueous asymmetric supercapacitors. *Nano Energy* **21**, 145–153 (2016).
46. Liu, J. et al. Advanced energy storage devices: basic principles, analytical methods, and rational materials design. *Adv. Sci.* **5**, 1700322 (2018).
47. Wang, X. et al. 2D/2D 1T-MoS_2/Ti_3C_2 MXene heterostructure with excellent supercapacitor performance. *Adv. Funct. Mater.* **30**, 0190302 (2020).
48. Suktha, P., Phattharasupakun, N., Dittanet, P. & Sawangphruk, M. Charge storage mechanisms of electrospun Mn_3O_4 nanofibres for high-performance supercapacitors. *RSC Adv.* **7**, 9958–9963 (2017).
49. Lin, Y. et al. Chromium-ruthenium oxide solid solution electrocatalyst for highly efficient oxygen evolution reaction in acidic media. *Nat. Commun.* **10**, 162 (2019).
50. Jeon, S. et al. RuO_2 nanorods on electrospun carbon nanofibers for supercapacitors. *ACS Appl. Nano Mater.* **3**, 3847–3858 (2020).
51. Kumar, R. et al. In situ carbon-supported titanium dioxide (ICS-TiO_2) as an electrode material for high performance supercapacitors. *Nanoscale Adv.* **2**, 2376–2386 (2020).
52. Luan, V. H., Han, J. H., Kang, H. W. & Lee, W. Highly porous and capacitive copper oxide nanowire/graphene hybrid carbon nanostructure for high-performance supercapacitor electrodes. *Compos. B. Eng.* **178**, 107464 (2019).
53. Zhu, G. et al. Highly conductive three-dimensional MnO_2–carbon nanotube–graphene–Ni hybrid foam as a binder-free supercapacitor electrode. *Nanoscale* **6**, 1079–1085 (2014).
54. Iqbal, N. et al. Flexible Fe_3O_4@carbon nanofibers hierarchically assembled with MnO_2 particles for high-performance supercapacitor electrodes. *Sci. Rep.* **7**, 15153 (2017).
55. Liu, Y. et al. CuO nanosheets/rGO hybrid lamellar films with enhanced capacitance. *Nanoscale* **5**, 9134–9140 (2013).
56. Saraf, M., Dar, R. A., Natarajan, K., Srivastava, A. K. & Mobin, S. M. A binder-free hybrid of CuO-microspheres and rGO nanosheets as an alternative material for next generation energy storage application. *ChemistrySelect* **1**, 2826–2833 (2016).